

JR2net: A Joint Non-Linear Representation and Recovery Network for Compressive Spectral Imaging

BRAYAN MONROY, JORGE BACCA, AND HENRY ARGUELLO*

Department of Systems Engineering, Universidad Industrial de Santander, Bucaramanga, Colombia

*henarfu@uis.edu.co

Abstract: Deep learning models are state-of-the-art in compressive spectral imaging (CSI) recovery. These methods use a deep neural network (DNN) as an image generator to learn non-linear mapping from compressed measurements to the spectral image. For instance, the deep spectral prior approach uses a convolutional autoencoder network (CAE) in the optimization algorithm to recover the spectral image by using a non-linear representation. However, the CAE training is detached from the recovery problem, which does not guarantee optimal representation of the spectral images for the CSI problem. This work proposes a joint non-linear representation and recovery network (JR2net), linking the representation and recovery task into a single optimization problem. JR2net consists of an optimization-inspired network following an ADMM formulation that learns a non-linear low-dimensional representation and simultaneously performs the spectral image recovery, trained via the end-to-end approach. Experimental results show the superiority of the proposed method with improvements up to 2.57 dB in PSNR and performance around 2000 times faster than state-of-the-art methods.

© 2022 Optica Publishing Group

1. Introduction

Spectral imaging senses spatial information along several wavelengths of the electromagnetic spectrum, which combines imaging and spectroscopy. Imaging consists of obtaining the spatial information of the scene by measuring the intensity of light emitted by objects. On the other hand, spectroscopy consists of sensing the spectral information of the object by measuring the response on the electromagnetic spectrum along multiple wavelengths [1]. Combining of these sub-fields enables spectral imaging systems to acquire spatial-spectral information of objects, which can be represented as a 3D data cube where two dimensions stand for the spatial information and the third for the spectral information [2]. Due to the importance of spectral information presented in objects, spectral images have been used in precision agriculture [3], medical imaging [4], remote sensing [5], and microscopy [1].

Several scanning methods have been explored for their potential to acquire spectral images. For instance, techniques such as whiskbroom, pushroom, and filtering changing sense spectral pixels, spectral lines, or spectral bands, respectively. However, these systems sequentially sense a subset of the data cube and thus require large sensing time to obtain a complete data cube [6–8]. Hence, based on compressive sampling (CS) theory [9], snapshot techniques have been proposed. For instance, snapshot spectral imaging systems such as coded aperture snapshot spectral imager (CASSI) based on single-disperser (SD-CASSI) [6] or dual-disperser (DD-CASSI) [10], employs coded apertures and dispersive elements to modulate the optical path from a scene. A detector captures a two-dimensional compressed projection of the three-dimensional data cube, reducing the amount of captured data [6]. This snapshot system describes an under-determined system where a recovery step is needed to recover an estimation of the 3D data cube from the compressed projection [11].

Compressive spectral optimization algorithms assume some prior information about the natural signal to solve the under-determined recovery problem and reduce the number of parameters to be recovered. For instance, due to the redundant spatial and spectral information presented in the scene, algorithms often assume a sparse representation on some orthonormal basis, such as Wavelet, discrete cosine transform (DCT) domain, and Kronecker-Wavelet [9, 12–14]. On the other hand, deep learning-based methods aim to learn a spectral prior as a non-linear representation of the spectral images, outperforming traditional sparse representation techniques. For instance, Autoencoder [15, 16] uses a convolutional autoencoder (CAE) to learn a non-linear representation of the spectral data in an off-line training, which is later included as spectral prior in the optimization algorithm. However, the choice of the linear representation or the learning of the non-linear representation is not designed for the specific recovery problem where it is finally used; therefore, it does not guarantee an optimal recovery of spectral data in the CSI problem.

Consequently, this paper presents JR2net, a joint non-linear representation and recovery network for compressive spectral imaging. JR2net is inspired by an ADMM formulation that links the representation and recovery problem into a single optimization problem. Each ADMM iteration is unrolled into a network stage that involves a convolution decoder to learn the non-linear low-dimensional (NLD) representation shared along the stages. Furthermore, this work proposes a learned gradient network to learn the derivative of the convolutional decoder, and we present a loss function inspired by CAEs incorporated into the end-to-end training procedure. Experimental results show the superiority of the proposed method with improvements up to 2.57 dB in PSNR and performance around 2000 times faster than state-of-the-art methods.

2. Related Work

2.1. Model-based Optimization

Traditional CS recovery algorithms are considered to be hand-crafted as they use expert knowledge of the signal as prior information. These methods are based on optimization techniques that consist of a data fidelity term and incorporate the hand-crafted prior as a l_0 or l_1 regularization term [17]. To name; [6, 18, 19] assume low total variation (TV), [9, 20] explore spatial sparsity on a given basis such as Wavelet and spectral sparsity DCT domain [9, 12, 13] or [21, 22] employ low-rank structures based on the linear mixture model. Examples of algorithms that use sparsity priors include the GPSR [17], ADMM [23], CSALSA [24], ISTA [25], and AMP [26] among others. In these algorithms, an auxiliary variable is incorporated in the optimization problem to alternately minimize the data fidelity term and the l_0 or l_1 regularization term, where the latter is solved by *projection operator* [17, 26] or a *proximal operator* [23–25]. However, these hand-crafted methods require expert knowledge of the scene to select which prior is more appropriate for this spectral scene. Consequently, they do not represent the wide variety and non-linearity of spectral image representations [27].

2.2. Model-based Optimization with Deep Priors

These methods are based on iterative techniques that replace the hand-crafted prior with a deep neural network (DNN) used to learn a deep prior of the spectral images. Non-data-driven approaches, [27, 28] proposed untrained DNN as a deep generative model (DGM) where the input of the network (denoted as latent space) passes through convolution operators to generate the image recovery. The weights of untrained DNN aim to minimize the Euclidean distance between the forward sensing operator of the DNN output and the compressed measurement. Plug-and-Play with convolutional neural networks (PnP-CNNs) replace the proximal operator with a pre-trained CNN [29–31]. Finally, Autoencoder [15] proposed pre-trained the DGM to learn a non-linear representation using a convolutional autoencoder which is then incorporated into the optimization problem. These methods replace the expert knowledge of the target with

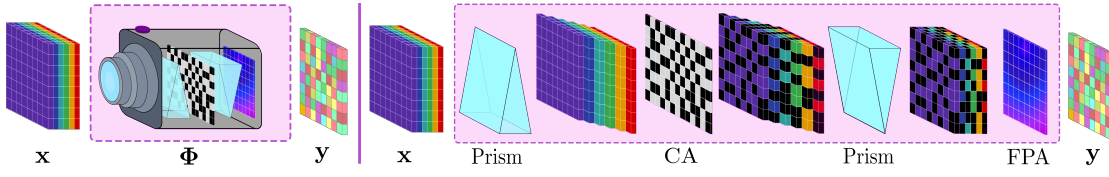


Fig. 1. (a) Dual Disperser DD-CASSI system. (b) The input spectral image \mathbf{x} is sheared along the spectrum, subsequently, the information is coded following the transmission function of the coded aperture (CA), creating a coded signal scene. The coded signal is unsheared, and finally, a focal plane array (FPA) is used to obtain the 2D compressed projections.

extensive use of data. Additionally, these iterative methods need a training step for the non-linear representation learning, which does not contemplate the optimization problem or the particular sensing system.

2.3. Deep-based Optimization

These methods propose a DNN, which performs the inverse mapping from the compressed measurements to the spectral image. For instance, [32] proposed a U-net-based network as non-linear mapping replacing the 2D for 3D convolutions, [33] learns a stacked auto-encoder, [34] applied convolution layers, and convolutional, residual, and fully connected layers are also used in [35–38]. However, changes in the sensing system can drastically affect the performance of these methods. Recently, a novel approach suggested unrolling the traditional optimization method and learning the proximal operators resulting in a deep interpretable decoder [39], with some authors, such as [39–41] replacing the soft-thresholding operator for a spatial-spectral network. These methods allow learning the optimization parameters within the weights network, using an end-to-end optimization [11, 42]. Although learning the proximal operator increases the robustness of the method against changes in the sensing system, it depends on the particular optimization problem, limiting its use in other representation problems, unlike non-linear representation learning methods [15].

3. Compressive Spectral Imaging

Compressive spectral imaging (CSI) encodes and projects the spatial-spectral information of the scene through optical elements, as shown in Fig. 1. For instance, the dual-disperser (DD-CASSI) architecture comprises two main optical elements: the coded aperture and the prism. Physically, a spectral scene $\mathbf{x}(i, j, k)$ is first collected by the objective lens, which is sheared along the spectrum by a prism, and then spatially encoded by a coded aperture $T(i, j)$. Subsequently, the encoded sheared scene is unsheared through a second prism, and finally, a focal plane array (FPA) is used to obtain the 2D compressed projections $\mathbf{y}(i, j)$. The resulting 2D compressed projections can be mathematically described as

$$\mathbf{y}(i, j) = \sum_{k=1}^C T_{(i+C-k, j)} \mathbf{x}(i, j, k). \quad (1)$$

Eqn. (1), can be re-written in matrix-vector form as

$$\mathbf{y} = \Phi \mathbf{x} + \boldsymbol{\eta}, \quad (2)$$

where $\mathbf{y} \in \mathbb{R}^{HW}$ and $\mathbf{x} \in \mathbb{R}^{HWC}$ are the vectorized representation of the 2D compressed projections and the spectral scene, respectively, with H, W as the spatial size, and C as the

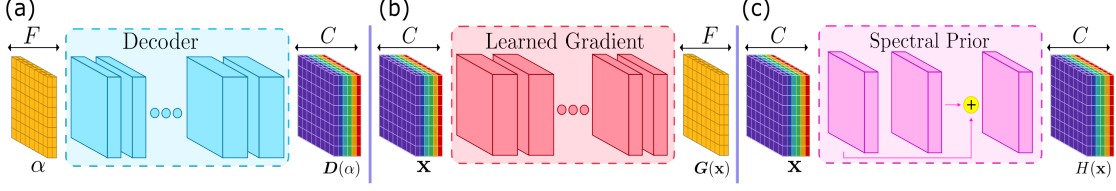


Fig. 2. (a) Decoder network and (b) learned gradient network composed of d -layered convolutional blocks. (c) The spectral prior network, consists of three convolutional blocks with a skip-connection. These three interpretable blocks were incorporated into the recovery algorithm.

number of spectral bands, $\Phi \in \mathbb{R}^{HW \times HWC}$ is the sensing matrix that describes the DD-CASSI image acquisition model, and $\eta \in \mathbb{R}^{HW}$ is the noise corruption inherent in the acquisition model. This equation describes a highly under-determined system, since $HW \ll HWC$.

4. Proposed Method

The proposed jointly representation and recovery method consists of an unrolled network inspired by an ADMM formulation. The unrolled network comprises three sub-blocks of interpretable layers, the decoder, the learned gradient network, and the spectral prior, shown in Fig. 2. The interpretable blocks are integrated into the optimization problem, where each one specializes in solving a specific problem. The decoder $D(\cdot)$ expands the NLD representation to the original spectral image. The learned gradient network $G(\cdot)$ learns the derivatives of the $D(\cdot)$ and simultaneously performs the non-linear transformation from the spectral images domain to the NLD representation domain. Finally, the spectral prior network $H(\cdot)$ learns a data-driven prior to further improve the spectral fidelity by substituting the proximal operator, which is explained in detail below.

4.1. Representation Learning

The representation learning consists in learn a non-linear representation $\alpha \in \mathbb{R}^{HWF}$ from a given spectral image $\mathbf{f} \in \mathbb{R}^{HWC}$, via the learning of a *decoder* $D(\cdot)$ which are composed of a set of convolutional layers and activations operators, as shown in Fig. 2(a). The decoder network expands the NLD representation to produce the original input data $\mathbf{x} \approx D(\alpha)$. Using the decoder network, the compressive image formation can be re-written as

$$\mathbf{y} = \Phi \mathbf{x} \approx \Phi D(\alpha), \quad (3)$$

Notice that when $HWF < HWC$, α is an NLD representation of the spectral image. For this work, we use the network architecture presented in [16], which will later be trained to guarantee an NLD representation.

4.2. Recovery Method

In order to recover the spectral image from the compressive measurements taking into account the NLD representation, we propose an unrolling method inspired by the following optimization problem

$$\underset{\alpha}{\text{minimize}} \quad \|\mathbf{y} - \Phi D(\alpha)\|_2^2 + \tau R(D(\alpha)), \quad (4)$$

where the first term is the data fidelity term, R is a prior term, and τ is the regularization parameter that controls the relative importance of the regularization term. The optimization problem in

Algorithm 1 ADMM Solution for the optimization problem in Eqn. (5)

Input: Φ, \mathbf{y}

- 1: $\alpha^{(0)} = \mathbf{G}(\Phi^\top \mathbf{y})$ ▷ LD representation initialization
- 2: $\mathbf{u}^{(0)} = 0$ ▷ auxiliary variable initialization
- 3: **while** not convergence **do**
- 4: $\nabla_\alpha \mathcal{L} = \mathbf{G}(\Phi^\top \Phi \mathbf{D}(\alpha) - \Phi^\top \mathbf{y}) + \rho \mathbf{G}(\mathbf{D}(\alpha) - \mathbf{h} + \mathbf{u})$
- 5: $\alpha^{(k+1)} = \alpha^{(k)} - \mu \nabla_\alpha \mathcal{L}$
- 6: $\mathbf{h}^{(k+1)} = \mathbf{H}^{(k+1)}(\mathbf{D}(\alpha^{(k+1)}) + \mathbf{u})$
- 7: $\mathbf{u}^{(k+1)} = \mathbf{u} + \mathbf{D}\alpha^{(k+1)} - \mathbf{h}^{(k+1)}$
- 8: **end while**
- 9: $\hat{\mathbf{x}} = \mathbf{D}(\alpha^{(k+1)})$ ▷ Spectral image recovery
- 10: **return** $\hat{\mathbf{x}}$

Eqn. (4) can be written as

$$\begin{aligned} & \underset{\alpha, \mathbf{h}}{\text{minimize}} && f(\alpha) + g(\mathbf{h}), \\ & \text{subject to} && \mathbf{D}(\alpha) = \mathbf{h}, \end{aligned} \quad (5)$$

where $f(\alpha) = \|\mathbf{y} - \Phi \mathbf{D}(\alpha)\|_2^2$ and $g(\mathbf{h}) = \tau R(\mathbf{D}(\alpha))$. Then, given the augmented Lagrangian in Eqn. (5) as

$$\mathcal{L}(\alpha, \mathbf{h}) = f(\alpha) + g(\mathbf{h}) + \frac{\rho}{2} \|\mathbf{D}(\alpha) - \mathbf{h} + \mathbf{u}\|_2^2, \quad (6)$$

where \mathbf{u} is an auxiliary variable, this problem can be solved using the alternating direction method of multipliers (ADMM), as shown in Algorithm (1). ADMM scheme consists of iteratively minimizing Eqn. (6) via the alternating solution of α, \mathbf{h} subproblems. The key points of this solution are summarized below. First the α -subproblem can be expressed as

$$\alpha^{(k+1)} = \arg \min_{\alpha} f(\alpha) + \frac{\rho}{2} \|\mathbf{D}(\alpha) - \mathbf{h} + \mathbf{u}\|_2^2, \quad (7)$$

due to fact that \mathbf{D} is a non-linear operator, it is not feasible to obtain a close-form solution for Eqn. (7). Instead, Eqn. (7) is solved using a gradient descent algorithm, following the gradients $\nabla_\alpha \mathcal{L}$ of the α -subproblem as

$$\begin{aligned} \nabla_\alpha \mathcal{L} = & \nabla_\alpha \mathbf{D}(\alpha) \cdot (\Phi^\top \Phi \mathbf{D}(\alpha) - \Phi^\top \mathbf{y}) \\ & + \rho \nabla_\alpha \mathbf{D}(\alpha) \cdot (\mathbf{D}(\alpha) - \mathbf{h} + \mathbf{u}), \end{aligned} \quad (8)$$

where $\Phi^\top \mathbf{y}$ represents the initialization. It is worth noting that the above expression involves computing the derivative of the decoder network with respect to the input $\nabla_\alpha \mathbf{D}(\alpha)$, which results in an expensive matrix calculation of $\mathbb{R}^{HWF \times HWC}$ dimensions. Therefore, we propose learning $\nabla_\alpha \mathbf{D}(\alpha)$ with the gradient network $\mathbf{G}(\cdot)$, such that, $\mathbf{G}(\cdot)$ aims to learn the derivative of the decoder network. So, Eqn. (8) can be re-written as

$$\nabla_\alpha \mathcal{L} \approx \mathbf{G}(\Phi^\top \Phi \mathbf{D}(\alpha) - \Phi^\top \mathbf{y}) + \rho \mathbf{G}(\mathbf{D}(\alpha) - \mathbf{h} + \mathbf{u}), \quad (9)$$

then, following the gradient descent update rule, the solution to Eqn. (7) can be expressed as

$$\alpha^{(k+1)} = \alpha^{(k)} - \mu \nabla_\alpha \mathcal{L}, \quad (10)$$

where μ is the step size in the gradient descent. Second, the \mathbf{h} -subproblem can be expressed as

$$\begin{aligned} \mathbf{h}^{(k+1)} &= \arg \min_{\mathbf{h}} g(\mathbf{h}^{(k)}) + \frac{\rho}{2} \|\mathbf{D}(\alpha^{(k+1)}) - \mathbf{h} + \mathbf{u}\|_2^2, \\ &= \arg \min_{\mathbf{h}} \tau R(\mathbf{h}^{(k)}) + \frac{\rho}{2} \|\mathbf{D}(\alpha^{(k+1)}) - \mathbf{h} + \mathbf{u}\|_2^2, \end{aligned} \quad (11)$$

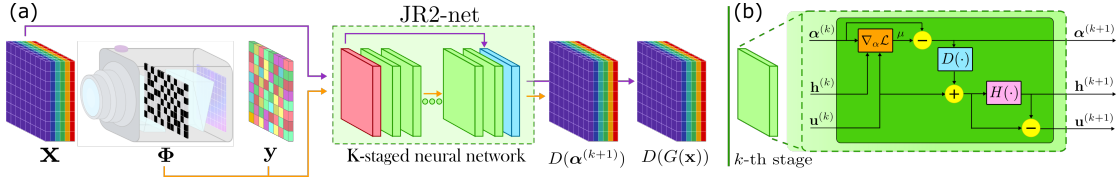


Fig. 3. (a) The proposed joint representation and recovery network architecture (JR2net).
(b) k -th stage into the JR2net, each stage represents an iteration of the Algorithm (1).
For the first stage, $\alpha^{(0)}$ is initialized as $G(\Phi^T \mathbf{y})$.

it can see that solution to Eqn. (11) is a proximal operator of the spectral image prior R with penalty τ [43]. When the spectral image prior uses the l_1 sparsity, the proximal operator implies a soft-thresholding on $D(\alpha^{(k+1)} + \mathbf{u})$. In this work, instead of explicitly learning a spectral image prior R and solving the operator with the constraint of the spectral image prior, we adopt the approach used in [39, 40] and learn a solver $H(\cdot)$ for the proximal operator with a spectral prior network, expressed as follows

$$\mathbf{h}^{(k+1)} = H(D(\alpha^{(k+1)} + \mathbf{u})). \quad (12)$$

The spectral prior network $H(\cdot)$ is a CNN composed of three convolutional block with a skip connection, as shown in Fig. 2(b). Finally, the auxiliary variable update

$$\mathbf{u}^{(k+1)} = \mathbf{u}^{(k)} + D(\alpha^{(k+1)}) - \mathbf{h}^{(k+1)}. \quad (13)$$

4.3. Joint Non-Linear Representation-Recovery Network

The ADMM scheme consists of iteratively applying the steps summarized in Algorithm (1) until a stop criterion is satisfied. The unrolling technique consists of unrolling K -iterations of the optimization algorithm into K stages of a DNN, in which each stage corresponds to one iteration in the optimization algorithm. This technique allows us to jointly learn both the network parameters and optimization parameters, which stabilizes training and improves the speed and accuracy of spectral images recovered [41, 44].

To learn the NLD representations and the recovery problem simultaneously, the Algorithm (1) is unrolled into a K -staged network as shown in Fig. 3. In this architecture, each k -stage of the unrolled network are composed of the $\alpha^{(k)}$, $\mathbf{h}^{(k)}$, $\mathbf{u}^{(k)}$ update steps. In order to learn a unique deep spectral representation, the sub-networks $G(\cdot)$, and $D(\cdot)$ are shared along the stages, which significantly reduces the parameters of the unrolled network. All the parameters in each stage are individually defined stage by stage, and $\mu^{(k)}$, $\rho^{(k)}$ and $H^{(k)}(\cdot)$ represent μ , ρ and $H(\cdot)$ at k -th stage. Once the network is built, we perform a end-to-end training into a set of spectral images and synthetic sensing matrices $\{\mathbf{x}^{(i)}, \Phi^{(i)}\}_{i=1}^N$, in order to learn the optimization parameters $\Omega = \{\mu^{(k)}, \rho^{(k)}\}_{k=1}^K$, the NLD representations and the network parameters for the recovery problem. Therefore, the complete objective for finding the optimal set of model parameters $\mathbf{Q}^* = \{D^*, G^*, H^{*(k)}, \Omega^*\}$ is given by

$$\mathbf{Q}^* = \arg \min_{\mathbf{Q}} \mathbb{E} \left[\|\hat{\mathbf{x}}^{(i)} - \mathbf{x}^{(i)}\|_2^2 \right], \quad (14)$$

where $\hat{\mathbf{x}} = U(\mathbf{y}, \Phi; \mathbf{Q})$ is the recovered spectral image from the unrolled network $U(\cdot)$ given the input sensor measurements \mathbf{y} , sensing matrix Φ , and the model parameters \mathbf{Q} .

4.4. Autoencoder Loss Function

CAEs consist of an *encoder* $E(\cdot)$ and a *decoder* $D(\cdot)$, where each operator is composed of a set of convolutional layers and activation operators [45]. The encoder network extracts the features and transforms the input data into a non-linear representation $\alpha = E(\mathbf{x})$, then the decoder network expands the NLD representation to produce the original input data $\mathbf{x} \approx D(\alpha)$. This type of network has been successfully applied in tasks such as image classification [46], image clustering [47], and denoising [48]. The forward model of the CAE can be mathematically expressed as

$$\mathbf{A}(\mathbf{x}) = D(E(\mathbf{x})) \approx \mathbf{x}. \quad (15)$$

Notice that, $E(\cdot)$ performs a non-linear transformation from the spectral images domain to the α domain, which is similar to the objective of the proposed learned gradient network $G(\cdot)$ in the proposed method. Therefore, inspired by the CAEs architectures and in order to optimize even more the NLD representation learning, we introduce the autoencoder loss function L_{ae} , which measures the error between the original and the autoencoder representation spectral images as

$$L_{ae} = \|\mathbf{x}^{(i)} - D(G(\mathbf{x}^{(i)}))\|_2^2. \quad (16)$$

Thus, the training loss function in Eqn. (14) can be re-written as

$$\mathbf{Q}^* = \arg \min_{\mathbf{Q}} \mathbb{E} \left[\|\hat{\mathbf{x}}^{(i)} - \mathbf{x}^{(i)}\|_2^2 + \lambda L_{ae} \right]. \quad (17)$$

We would like to highlight that instead of pre-training a convolutional autoencoder into a spectral image dataset and then training a second network for the image recovery, the proposed model jointly learns the NLD representations of spectral images and recovers them from these representations; in this sense, the $G(\cdot)$ aims to learn the derivatives of the decoder $\nabla_{\alpha} D(\cdot)$ and the non-linear mapping from the NLD representation at the same time. This can be done by including the autoencoder representation loss L_{ae} into the training procedure.

4.5. Computational Complexity

With regard to the computational complexity of Algorithm 1, the most costly steps are the forward pass of $E(\cdot)$ in Line 4, which are the order of complexity $O(HWF_{max})$, where F_{max} is the convolutional layer with maximum number of filters. The matrix multiplication by Φ and Φ^T can be performed element-wise due to definition in Eqn. (1), and thus has an order of complexity $O(HWC)$. Therefore, the overall order of complexity per iteration is given by $O(HWF_{max}) + O(HWC)$. Finally, Algorithm 1 has computational complexity $O(N_k HWF_{max}) + O(N_k HWC)$ where N_k is the number of stages in the unrolled network.

5. Simulations on Synthetic Data

5.1. Experimental Setup

The performance of the proposed method was evaluated on two hyperspectral image datasets (KAIST [15], and ARAD [49]). Each dataset contained 31 spectral bands and was down-sampled to 512×512 spatial resolution. The datasets are composed of 30 and 460 images and were divided into 27/3 and 450/10 images, respectively, for training and testing [16, 50]. The simulated acquisition system was the Dual Disperser DD-CASSI.



Fig. 4. Ablation study, influence of the \mathcal{L}_{ae} loss function into the recovery performance.

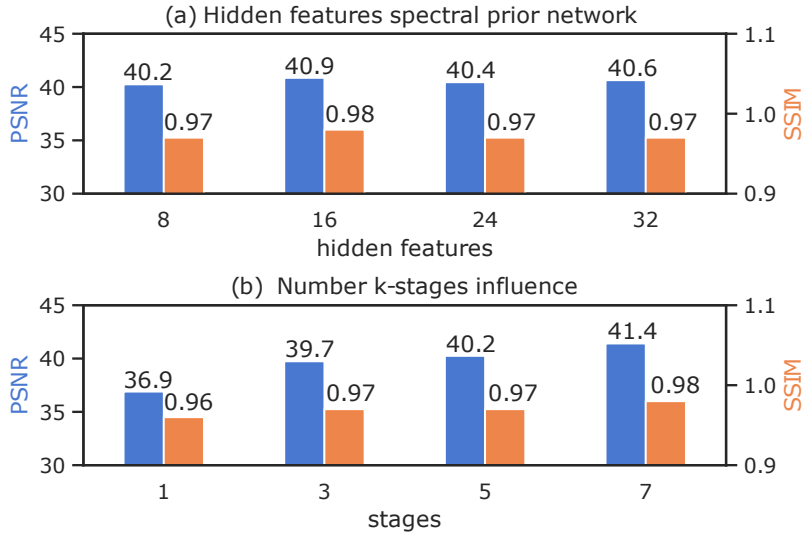


Fig. 5. Network configuration. (a) Influence of the amount of hidden features for the spectral prior network, (b) Influence of amount of stages of the unrolled network.

For the training procedure, a data augmentation scheme is employed to avoid overfitting, which consists of randomly extracting 24 spectral patches of 96x96x31 resolution for each spectral image along with the training steps. Additionally, randomly coded apertures of 0.3 transmittance are generated along training steps to obtain a synthetic 2D compressed projection for each spectral patch. The training configurations are composed of 3000 training epochs with 104 batch-size, 10^{-3} as learning rate with the Adam optimizer, running on an RTX 3090 GPU with 24 GDDR6 VRAM. The quality of the spectral image estimation was evaluated using the peak signal-to-noise ratio (PSNR), structural similarity index measure (SSIM), and spectral angle mapper (SAM) metrics.

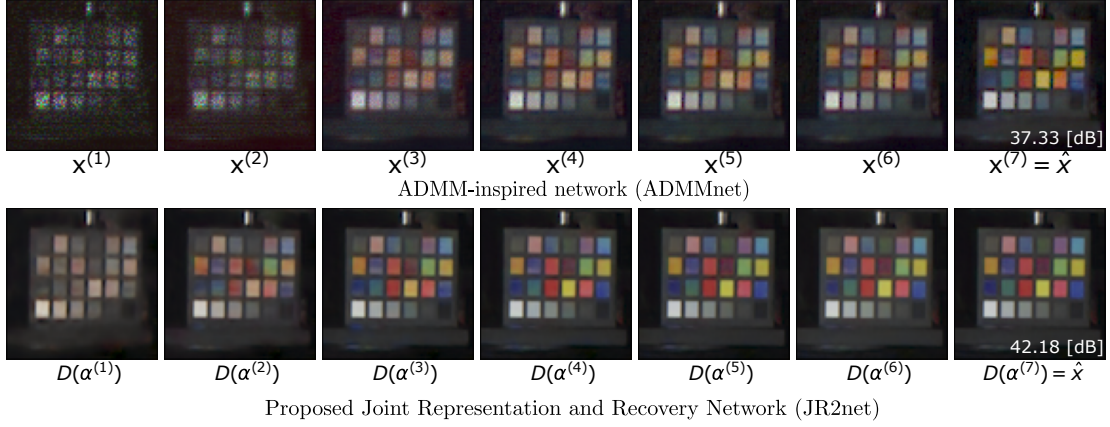


Fig. 6. Intermediate outputs along unrolled stages obtained by ADMMnet and proposed JR2net, with each column corresponding to the k -th stage estimation of the spectral image. The ADMMnet is the case when $\mathbf{D}(\cdot)$ and $\mathbf{G}(\cdot)$ are identity operators, namely $\mathbf{D}(\cdot) = \mathbf{G}(\cdot) = \mathbf{I}$.

5.2. Network Configuration

The baseline configuration of the proposed network consists of a $\mathbf{D}(\cdot)$ and $\mathbf{G}(\cdot)$ of 5 hidden layers with an NLD representation of 8 features, as suggested in our previous work [16]. The spectral prior network is a convolutional residual network following the architecture suggested by authors in [39]. To verify the effectiveness of introducing the \mathcal{L}_{ae} into the training procedure of the NLD representation learning, an ablation study was conducted on the KAIST dataset. Experimental results show that introducing the \mathcal{L}_{ae} loss function increases the recovery quality by around 3 dB of PSNR, as shown in Figure (4). Thus, it can be verified that regularizing the $\mathbf{G}(\cdot)$ network via the proposed loss function \mathcal{L}_{ae} that simultaneously learns the derivatives of the decoder network and the non-linear transformation as an encoder network in CAE architectures, further increasing the global performance of the proposed network.

Furthermore, the influence of the number of stages of the unrolled network and hidden features for the prior spectral network was evaluated on the PSNR and SSIM metrics. First, the proposed method was evaluated for a different number of hidden features $\{8, 16, 24, 32\}$ in the spectral prior network $\mathbf{H}(\cdot)$ with a fixed number of 5 stages. As can be seen in Fig. 5(a), there is no significant increase in performance for hidden features greater than 16. Second, the proposed method was evaluated for different models of different numbers of stages with $k = \{1, 3, 5, 7\}$ and a fixed number of 8 hidden features. As can be seen in Fig. 5(b), as the number of stages increases, the performance of the recovery is increased, achieving the best performance for a value of $k = 7$. Therefore, based on simulation results, the network configuration with optimal cost and performance consists of $k = 7$ stages of the unrolled network and 16 hidden features for the spectral prior network.

5.3. Performance Evaluation

We evaluated the influence of NLD representation learning. For this, the proposed method was compared for the case when the decoder and learned gradient network are the identity operator ($\mathbf{D}(\cdot) = \mathbf{G}(\cdot) = \mathbf{I}$). In this case, the proposed method becomes the ADMMnet [41]. Intermediate outputs of the spectral image estimations for the ADMMnet, as well as the proposed JR2net for the configuration of $k = 7$ stages, are shown in Fig. 6.



Fig. 7. Recovery results: PnP [29], DNU [40], DIP [27], ADMMnet [41], LDSR [16], and the proposed method for two tested images on the KAIST and ARAD dataset. The numbers in parenthesis show the averaged PSNRs and SSIMs scores.

Metric	PSNR			SSIM			SAM		
	40	30	25	40	30	25	40	30	25
ADMMnet	37.81	37.34	36.16	0.960	0.949	0.925	0.175	0.222	0.276
JR2net	40.29	40.05	37.13	0.982	0.965	0.918	0.115	0.177	0.248

Table 1. Mean performance comparison for the proposed method and ADMMnet under different levels of noise. Best values are labeled in bold.

Dataset	KAIST			ARAD			GPU Time [s]
	PSNR	SSIM	SAM	PSNR	SSIM	SAM	
PnP	29.79	0.917	0.190	31.51	0.851	0.120	263.9
DNU	32.60	0.917	0.230	29.54	0.830	0.140	0.357
DIP	32.79	0.920	0.220	35.78	0.958	0.080	441.5
ADMMnet	37.87	0.963	0.160	33.45	0.904	0.100	0.185
LDSR	<u>38.84</u>	<u>0.977</u>	<u>0.110</u>	<u>38.23</u>	<u>0.968</u>	0.050	633.1
JR2net	41.41	0.984	0.100	39.65	0.977	0.050	<u>0.326</u>

Table 2. Performance comparison of the KAIST and ARAD datasets. The best performance is labeled in bold and the second best performance is underlined.

For ADMMnet results, the recovered image is gradually reduced in noise with the progression of the stages, which allows the $H(\cdot)$ sub-network to be interpreted as a denoiser, which is in concordance with the PnP methodology. Additionally, a good estimation can be observed from the first iteration, which shows an excellent estimation of the spatial information in the scene for the proposed method. The proposed model gradually improves spectral precision to achieve spectral image recovery. Additionally, the ADMMnet method and the proposed method were simulated under different levels of additive Gaussian noise $\{40, 30, 25\}$ dBs, with the results of this simulation being shown in Table (1). The proposed method presents the best results in all the metrics for the proposed noise values, presenting optimal performance results for SNR values greater than 30 dB. In this sense, learning an NLD representation of spectral images allows one to obtain a better estimation in terms of spatial structure and estimation with less noise in the first stages of the algorithm, significantly improving the final performance.

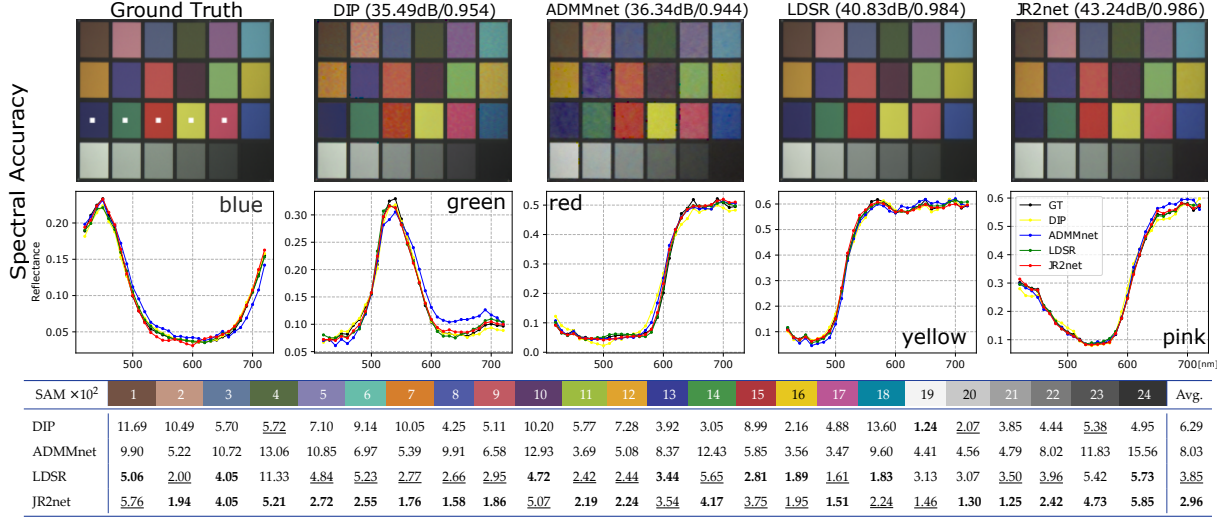


Fig. 8. Comparison of spectral accuracy of our spectral image recovery against three state-of-the-art methods: (a) DIP, (b) ADMMnet, and (c) LDSR. Numbers in parentheses on top of the pictures show the average across spectral bands PSSIM and SSIM scored between the recovery result and the ground truth. The middle row shows recovered reflectances for five color squares: blue, green, red, yellow, and pink. The bottom row shows the SAM score of the recovered spectra for the 24 color squares.

We compared the proposed method with state-of-the-art methods in compressive image recovery such as the Deep Non-Local Unrolling (DNU) [40], Plug and Play (PnP) [29], Deep Image Prior (DIP) [27], ADMM-inspired network (ADMMnet) [41], and low-dimensional spectral reconstruction (LDSR) [16]. PnP, DIP, and LDSR are model-based optimization methods, and DNU and ADMMnet are deep-based optimization methods. DNU, PnP, and ADMMnet do not employ representation learning, while LDSR learns a non-linear representation detached from the recovery problem. All methods were implemented according to the hyperparameters suggested by the authors. Fig. 7 shows an RGB false color for three recovered spectral images on the KAIST and ARAD test datasets. Quantitative results are shown in Table (2); it can be seen that the proposed method outperforms the fastest method (ADMMnet) by 1.41 dB and 2.57 dB on KAIST and ARAD, respectively, and is around 2000 times faster than the second method with the best recovery accuracy (LDSR), which indicates a significant improvement in terms of accuracy and speed. The gain in recovery speed is because once the network is trained, the recovery of the spectral image is performed in a single forward step, requiring 0.326 seconds to recover each new measurement. Additionally, it is worth highlighting that the proposed method does not need to include a sparse representation constraint to achieve an optimal recovery quality, unlike the Wavelet basis used in LDSR.

Finally, Fig. 8 shows a comparison of the individual spectral accuracy of the state-of-the-art and the proposed method. The top row shows comparisons for the ColorChecker spectral image from the KAIST dataset. The middle row shows the recovered spectral reflectances of five color squares in the chart: blue, green, red, yellow, and pink; our results are consistent with the spectral response of the ground truth. The table at the bottom shows the SAM score for each color square and the average.

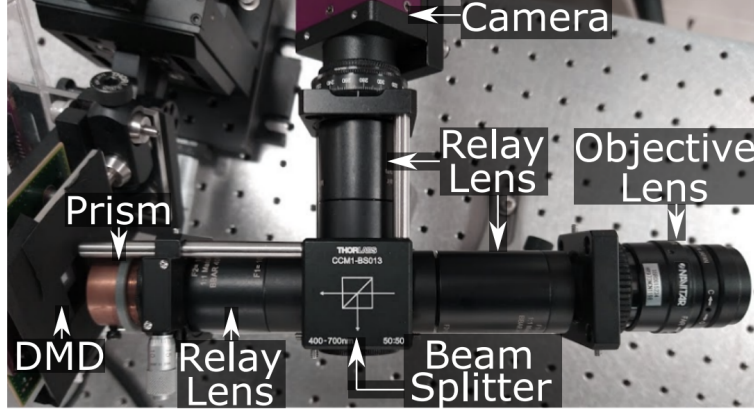


Fig. 9. Testbed DD-CASSI imaging system implementation.

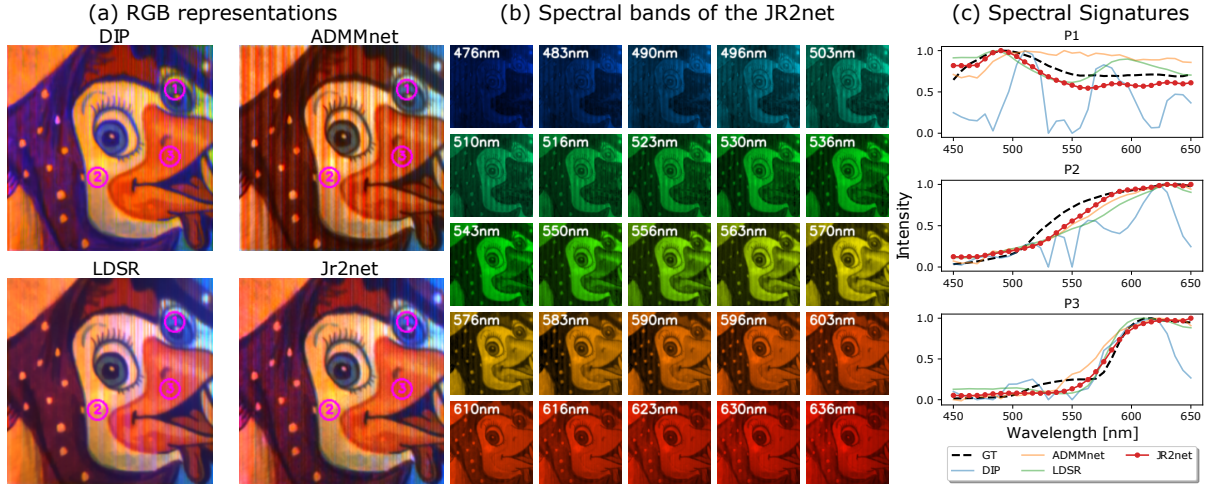


Fig. 10. (a) RGB representation of the scene obtained with different methods and the proposed method. (b) Spectral band representations of 25 recovered spectral bands for the proposed method. (c) Normalized spectral signatures of the three points shown in Fig. 10(a), compared with the spectrum acquired by a spectrometer.

5.4. Validation in Real Measurements

We evaluated the proposed method with real measurements provided by authors in [51] using a testbed implementation of a spatial-spectral DD-CASSI imaging system, shown in Fig. 9. The system uses a Navitar lens (12mm FixedFocal Length, MVL12M23 - 12mm EFL, $f/1.4$) as the objective lens, two matched achromatic doublet pair relay lens (Thorlabs MAP10100100-A, $f_1 = 100.0mm$, $f_2 = 100.0mm$), a double Amici prism coupled to a rotation mount (Thorlabs CRM1P, 30mm cage rotation mount, 1"), a digital mirror decide (DMD, Texas Instruments, D4120), a beam splitter (BS), a third matched achromatic doublet pair relay lens (Thorlabs MAP105050-A, $f_1 = 50.0mm$, $f_2 = 50.0mm$), and a sensor (Stingray F-0980B, $4.65\mu m$ pixel size).

The compressed projection and spectral image have a spatial resolution of 256×256 pixels with characterization to recover up to $C = 31$ spectral bands. The coded aperture designed in [51] is generated from a random binary pattern with 18% transmittance and acquires three snapshots. Based on the performance evaluation summarized in Table 2, DIP, ADMMnet, LDSR, and the proposed method are selected for the real data validation.

Fig. 10(a) presents a false-colored RGB of recovered spectral images obtained via the CIE RGB color matching functions [52] for visualization. Fig. 10(b) presents the spectral band representation of 25 spectral bands recovered for the proposed method. It can be seen that the proposed method obtains an optimal estimation of the spatial information. Furthermore, the spectral response of three particular spatial points in the scene, indicated as a magenta circle in the images, is compared with a spectrometer (Ocean Optics Flame S-VIR-NIR-ES spectrometer), as shown in Fig. 10(c). Our results show that the proposed method has a better estimation of the spatial and spectral information, and the spectral signatures are closer to the ones taken by the spectrometer. Notice that using an NLD representation in the unrolling network allows us to successfully estimate the response to the spectrum, unlike the ADMMnet method. The strategy of jointly learning the NLD representation with the recovery problem outperforms the pre-training approach. All computations were conducted using an NVIDIA Tesla K80 with 12GB of GDDR5 memory. The computation time of the JR2net was about 0.2 seconds. Code implementation can be found in [53].

6. Conclusions

This work proposes a joint non-linear representation and recovery network (JR2net) for the compressive spectral imaging problem. The JR2net contemplates the sensing systems and optimizes the learning of the non-linear low-dimensional representation for the recovery problem. The learned gradient network and the new autoencoder loss function reduce the computational complexity and increase recovery quality. This contribution relies on optimal estimations from the first stages of the unrolled network. Consequently, the proposed method outperforms state-of-the-art methods in terms of accuracy and speed, being around 2000 times faster than LDSR, the second method with the best recovery accuracy, and 2.57 dB above ADMMnet, the method with the best speed. The recovery results in real data that validates the performance of the proposed method for a DD-CASSI setup using a binary-coded aperture.

7. Acknowledgment

The authors acknowledge the Vicerrectoría de Investigación y Extension of Universidad Industrial de Santander for supporting this work with the project number 2793, and the program "Desarrollo de algoritmos de aprendizaje profundo basados en arquitecturas de extremo a extremo para la solución de problemas inversos".

8. Disclosures

The author declares no conflicts of interest.

References

1. Y. Garini, I. T. Young, and G. McNamara, "Spectral imaging: principles and applications," *Cytom. Part A: The J. Int. Soc. for Anal. Cytol.* **69**, 735–747 (2006).
2. J. L. Bacca and H. Arguello, "Sparse subspace clustering in hyperspectral images using incomplete pixels," *Tecnológicas* **22**, 1–14 (2019).
3. D. Caballero, R. Calvini, and J. M. Amigo, "Hyperspectral imaging in crop fields: precision agriculture," in *Data Handling in Science and Technology*, vol. 32 (Elsevier, 2020), pp. 453–473.
4. B. Fei, "Chapter 3.6 - hyperspectral imaging in medical applications," in *Hyperspectral Imaging*, vol. 32 of *Data Handling in Science and Technology* J. M. Amigo, ed. (Elsevier, 2020), pp. 523 – 565.

5. M. Borengasser, W. S. Hungate, and R. Watkins, *Hyperspectral remote sensing: principles and applications* (CRC press, 2007).
6. A. Wagadarikar, R. John, R. Willett, and D. Brady, "Single disperser design for coded aperture snapshot spectral imaging," *Appl. optics* **47**, B44–B51 (2008).
7. L. Gao, J. Liang, C. Li, and L. V. Wang, "Single-shot compressed ultrafast photography at one hundred billion frames per second," *Nature* **516**, 74–77 (2014).
8. J. Liang and L. V. Wang, "Single-shot ultrafast optical imaging," *Optica* **5**, 1113–1127 (2018).
9. E. J. Candes and M. B. Wakin, "An introduction to compressive sampling," *IEEE Signal Process. Mag.* **25**, 21–30 (2008).
10. M. E. Gehm, R. John, D. J. Brady, R. M. Willett, and T. J. Schulz, "Single-shot compressive spectral imaging with a dual-disperser architecture," *Opt. Express* **15**, 14013–14027 (2007).
11. J. Bacca, T. Gelvez-Barrera, and H. Arguello, "Deep coded aperture design: An end-to-end approach for computational imaging tasks," *IEEE Transactions on Comput. Imaging* **7**, 1148–1160 (2021).
12. Y. Fu, Y. Zheng, I. Sato, and Y. Sato, "Exploiting spectral-spatial correlation for coded hyperspectral image restoration," in *Proceedings of the IEEE Conference on Computer Vision and Pattern Recognition*, (2016), pp. 3727–3736.
13. L. Wang, Z. Xiong, G. Shi, F. Wu, and W. Zeng, "Adaptive nonlocal sparse representation for dual-camera compressive hyperspectral imaging," *IEEE transactions on pattern analysis machine intelligence* **39**, 2104–2111 (2016).
14. M. F. Duarte and R. G. Baraniuk, "Kronecker compressive sensing," *IEEE Transactions on Image Process.* **21**, 494–504 (2011).
15. I. Choi, D. S. Jeon, G. Nam, D. Gutierrez, and M. H. Kim, "High-quality hyperspectral reconstruction using a spectral prior," *ACM Trans. Graph.* **36** (2017).
16. B. Monroy, J. Bacca, and H. Arguello, "Deep low-dimensional spectral image representation for compressive spectral reconstruction," in *2021 IEEE 31st International Workshop on Machine Learning for Signal Processing (MLSP)*, (IEEE, 2021), pp. 1–6.
17. M. A. Figueiredo, R. D. Nowak, and S. J. Wright, "Gradient projection for sparse reconstruction: Application to compressed sensing and other inverse problems," *IEEE J. selected topics signal processing* **1**, 586–597 (2007).
18. Y. Wang, J. Yang, W. Yin, and Y. Zhang, "A new alternating minimization algorithm for total variation image reconstruction," *SIAM J. Imaging Sci.* **1**, 248–272 (2008).
19. J. M. Bioucas-Dias and M. A. T. Figueiredo, "A new twist: Two-step iterative shrinkage/thresholding algorithms for image restoration," *IEEE Transactions on Image Process.* **16**, 2992–3004 (2007).
20. C. V. Correa, H. Arguello, and G. R. Arce, "Snapshot colored compressive spectral imager," *JOSA A* **32**, 1754–1763 (2015).
21. J. Bacca, C. V. Correa, and H. Arguello, "Noniterative hyperspectral image reconstruction from compressive fused measurements," *IEEE J. Sel. Top. Appl. Earth Obs. Remote. Sens.* **12**, 1231–1239 (2019).
22. T. Gelvez, H. Rueda, and H. Arguello, "Joint sparse and low rank recovery algorithm for compressive hyperspectral imaging," *Appl. optics* **56**, 6785–6795 (2017).
23. S. Boyd, N. Parikh, and E. Chu, *Distributed optimization and statistical learning via the alternating direction method of multipliers* (Now Publishers Inc, 2011).
24. M. V. Afonso, J. M. Bioucas-Dias, and M. A. Figueiredo, "An augmented lagrangian approach to the constrained optimization formulation of imaging inverse problems," *IEEE Transactions on Image Process.* **20**, 681–695 (2010).
25. A. Beck and M. Teboulle, "A fast iterative shrinkage-thresholding algorithm for linear inverse problems," *SIAM journal on imaging sciences* **2**, 183–202 (2009).
26. D. L. Donoho, A. Maleki, and A. Montanari, "Message-passing algorithms for compressed sensing," *Proc. Natl. Acad. Sci.* **106**, 18914–18919 (2009).
27. J. Bacca, Y. Fonseca, and H. Arguello, "Compressive spectral image reconstruction using deep prior and low-rank tensor representation," *Appl. Opt.* **60**, 4197–4207 (2021).
28. D. Ulyanov, A. Vedaldi, and V. Lempitsky, "Deep image prior," *Int. J. Comput. Vis.* **128**, 1867–1888 (2020).
29. X. Yuan, Y. Liu, J. Suo, and Q. Dai, "Plug-and-play algorithms for large-scale snapshot compressive imaging," in *Proceedings of the IEEE/CVF Conference on Computer Vision and Pattern Recognition*, (2020), pp. 1447–1457.
30. S. H. Chan, X. Wang, and O. A. Elgendy, "Plug-and-play admm for image restoration: Fixed-point convergence and applications," *IEEE Transactions on Comput. Imaging* **3**, 84–98 (2016).
31. J. Rick Chang, C.-L. Li, B. Póczos, B. Vijaya Kumar, and A. C. Sankaranarayanan, "One network to solve them all—solving linear inverse problems using deep projection models," in *Proceedings of the IEEE International Conference on Computer Vision*, (2017), pp. 5888–5897.
32. D. Gedalin, Y. Oiknine, and A. Stern, "Deepcubenet: reconstruction of spectrally compressive sensed hyperspectral images with deep neural networks," *Opt. express* **27**, 35811–35822 (2019).
33. A. Mousavi, A. B. Patel, and R. G. Baraniuk, "A deep learning approach to structured signal recovery," in *2015 53rd annual allerton conference on communication, control, and computing (Allerton)*, (IEEE, 2015), pp. 1336–1343.
34. A. Mousavi and R. G. Baraniuk, "Learning to invert: Signal recovery via deep convolutional networks," in *2017 IEEE international conference on acoustics, speech and signal processing (ICASSP)*, (IEEE, 2017), pp. 2272–2276.
35. A. Dave, A. K. Vadathya, R. Subramanyam, R. Baburajan, and K. Mitra, "Solving inverse computational imaging problems using deep pixel-level prior," *IEEE Transactions on Comput. Imaging* **5**, 37–51 (2018).
36. H. Palangi, R. Ward, and L. Deng, "Distributed compressive sensing: A deep learning approach," *IEEE Transactions*

- on Signal Process. **64**, 4504–4518 (2016).
37. H. Yao, F. Dai, S. Zhang, Y. Zhang, Q. Tian, and C. Xu, “Dr2-net: Deep residual reconstruction network for image compressive sensing,” *Neurocomputing* **359**, 483–493 (2019).
38. K. Kulkarni, S. Lohit, P. Turaga, R. Kerviche, and A. Ashok, “Reconnet: Non-iterative reconstruction of images from compressively sensed measurements,” in *Proceedings of the IEEE Conference on Computer Vision and Pattern Recognition*, (2016), pp. 449–458.
39. L. Wang, C. Sun, Y. Fu, M. H. Kim, and H. Huang, “Hyperspectral image reconstruction using a deep spatial-spectral prior,” in *Proceedings of the IEEE/CVF Conference on Computer Vision and Pattern Recognition (CVPR)*, (2019).
40. L. Wang, C. Sun, M. Zhang, Y. Fu, and H. Huang, “Dnu: Deep non-local unrolling for computational spectral imaging,” in *Proceedings of the IEEE/CVF Conference on Computer Vision and Pattern Recognition (CVPR)*, (2020).
41. Y. Sogabe, S. Sugimoto, T. Kurozumi, and H. Kimata, “Admm-inspired reconstruction network for compressive spectral imaging,” in *2020 IEEE International Conference on Image Processing (ICIP)*, (IEEE, 2020), pp. 2865–2869.
42. V. Sitzmann, S. Diamond, Y. Peng, X. Dun, S. Boyd, W. Heidrich, F. Heide, and G. Wetzstein, “End-to-end optimization of optics and image processing for achromatic extended depth of field and super-resolution imaging,” *ACM Transactions on Graph. (TOG)* **37**, 1–13 (2018).
43. S. Boyd, S. P. Boyd, and L. Vandenberghe, *Convex optimization* (Cambridge university press, 2004).
44. R. Liu, X. Fan, S. Cheng, X. Wang, and Z. Luo, “Proximal alternating direction network: A globally converged deep unrolling framework,” in *Thirty-Second AAAI Conference on Artificial Intelligence*, (2018).
45. J. Masci, U. Meier, D. Cireşan, and J. Schmidhuber, “Stacked convolutional auto-encoders for hierarchical feature extraction,” in *International conference on artificial neural networks*, (Springer, 2011), pp. 52–59.
46. Y. Zhang, K. Lee, and H. Lee, “Augmenting supervised neural networks with unsupervised objectives for large-scale image classification,” in *International conference on machine learning*, (PMLR, 2016), pp. 612–621.
47. K. Ghasedi Dizaji, A. Herandi, C. Deng, W. Cai, and H. Huang, “Deep clustering via joint convolutional autoencoder embedding and relative entropy minimization,” in *Proceedings of the IEEE international conference on computer vision*, (2017), pp. 5736–5745.
48. L. Gondara, “Medical image denoising using convolutional denoising autoencoders,” in *2016 IEEE 16th international conference on data mining workshops (ICDMW)*, (IEEE, 2016), pp. 241–246.
49. B. Arad, R. Timofte, O. Ben-Shahar, Y.-T. Lin, and G. D. Finlayson, “Ntire 2020 challenge on spectral reconstruction from an rgb image,” in *Proceedings of the IEEE/CVF Conference on Computer Vision and Pattern Recognition Workshops*, (2020), pp. 446–447.
50. H. Arguello, S. Pinilla, Y. Peng, H. Ikoma, J. Bacca, and G. Wetzstein, “Shift-variant color-coded diffractive spectral imaging system,” *Optica* **8**, 1424–1434 (2021).
51. J. Monsalve, M. Marquez, I. Esnaola, and H. Arguello, “Compressive covariance matrix estimation from a dual-dispersive coded aperture spectral imager,” in *2021 IEEE International Conference on Image Processing (ICIP)*, (IEEE, 2021), pp. 2823–2827.
52. C. Wyman, P.-P. Sloan, and P. Shirley, “Simple analytic approximations to the cie xyz color matching functions,” *J. Comput. Graph. Tech* **2**, 11 (2013).
53. B. Monroy, “Jr2net,” <https://github.com/hdspgroup/JR2net> (2022).